IJMMM International Journal of Minerals, Metallurgy and Materials 矿物冶金与材料学报（英文版）

Insights into the effects of Mn substitution in $CoFe_2O_4$ nanoferrites involving high-frequency storage device applications

Biswajita Dash, Krutika L. Routray, Sunirmal Saha, P.M. Sarun, and Subhasis Sarangi

Cite this article as:
Biswajita Dash, Krutika L. Routray, Sunirmal Saha, P.M. Sarun, and Subhasis Sarangi, Insights into the effects of Mn substitution in $CoFe_2O_4$ nanoferrites involving high-frequency storage device applications, *Int. J. Miner. Metall. Mater.*, 32(2025), No. 5, pp. 1245-1258. https://doi.org/10.1007/s12613-024-3040-3

View the article online at SpringerLink or IJMMM Webpage.

Articles you may be interested in

Bin Shi, Hongsheng Liang, Zijun Xie, Qing Chang, and Hongjing Wu, Dielectric loss enhancement induced by the microstructure of $CoFe_2O_4$ foam to realize broadband electromagnetic wave absorption, *Int. J. Miner. Metall. Mater.*, 30(2023), No. 7, pp. 1388-1397. https://doi.org/10.1007/s12613-023-2599-4

Xingliang Chen, Di Lan, Luoting Zhou, Hailing Liu, Xiyu Song, Shouyu Wang, Zhuanyong Zou, and Guanglei Wu, Review of recent advances in ferrite-based materials: From synthesis techniques to electromagnetic wave absorption performance, *Int. J. Miner. Metall. Mater.*, 32(2025), No. 3, pp. 591-608. https://doi.org/10.1007/s12613-024-3063-9

Lianggui Ren, Yiqun Wang, Xin Zhang, Qinchuan He, and Guanglei Wu, Efficient microwave absorption achieved through *in situ* construction of core–shell $CoFe_2O_4$@mesoporous carbon hollow spheres, *Int. J. Miner. Metall. Mater.*, 30(2023), No. 3, pp. 504-514. https://doi.org/10.1007/s12613-022-2509-1

Yuying Huo, Zhengyan Wang, Yanlan Zhang, and Yongzhen Wang, High-entropy ferrite with tunable magnetic properties for excellent microwave absorption, *Int. J. Miner. Metall. Mater.*, 32(2025), No. 3, pp. 668-677. https://doi.org/10.1007/s12613-024-2883-y

Bo Li, Lin Ma, Sinan Li, Jiewu Cui, Xiaohui Liang, Wei Sun, Pengjie Zhang, Nan Huang, Song Ma, and Zhidong Zhang, Electromagnetic wave absorption and corrosion resistance performance of carbon nanoclusters/Ce–Mn codoped barium ferrite composite materials, *Int. J. Miner. Metall. Mater.*, 32(2025), No. 3, pp. 699-709. https://doi.org/10.1007/s12613-024-2997-2

Yuanchun Zhang, Shengtao Gao, Xingzhao Zhang, Dacheng Ma, Chuanlei Zhu, and Jun He, Structural and microwave absorption properties of $CoFe_2O_4$/residual carbon composites, *Int. J. Miner. Metall. Mater.*, 32(2025), No. 1, pp. 221-232. https://doi.org/10.1007/s12613-024-2849-0

IJMMM WeChat

QQ author group

INTERNATIONAL JOURNAL OF
Minerals, Metallurgy and Materials

Volume 32, Number 5, May 2025
Page 1245

Research Article https://doi.org/10.1007/s12613-024-3040-3

Insights into the effects of Mn substitution in $CoFe_2O_4$ nanoferrites involving high-frequency storage device applications

Biswajita Dash[1)], *Krutika L. Routray*[1)], *Sunirmal Saha*[1),✉], *P.M. Sarun*[2)], *and Subhasis Sarangi*[2)]

1) Department of Physics, C.V. Raman Global University, Bhubaneswar 752054, India

2) Functional Ceramics Laboratory, Department of Physics, Indian Institute of Technology (Indian School of Mines), Dhanbad 826004, India

(Received: 13 September 2024; revised: 28 October 2024; accepted: 3 November 2024)

Abstract: Nanoferrites of the $CoMn_xFe_{(2-x)}O_4$ series (x = 0.00, 0.05, 0.10, 0.15, 0.20) were synthesized in this study using the sol–gel auto-combustion approach. The lattice constants were computed within the range of 8.312–8.406 Å, while crystallite sizes were estimated to range between 55.20 and 31.40 nm using the Scherrer method. The different functional groups were found to correlate with various absorption bands using Fourier transform infrared (FTIR) spectroscopy. Five active modes were identified by Raman spectroscopy, revealing vibration modes of O^{2-} ions at tetrahedral and octahedral locations. The ferromagnetic hysteresis loop was observed in all the synthesized samples, which can be explained by Neel's model. The results showed that AC conductivity decreased with increasing Mn^{2+} content at the Fe^{2+} site, while the dielectric constant and dielectric loss increased with increasing frequency. Furthermore, the saturation magnetization (M_s), remnant magnetization (M_r), and coercivity (H_c) all showed declining trends with the increase in Mn^{2+} doping. Finally, the $CoMn_{0.20}Fe_{1.8}O_4$ samples showed M_s and M_r values ranging from 73.12 to 66.84 emu/g and from 37.77 to 51.89 emu/g, respectively, while H_c values ranged from 1939 to 1312 Oe, after which coercivity increased. Thus, the $CoMn_{0.20}Fe_{1.8}O_4$ sample can be considered a promising candidate for magnetic applications.

Keywords: nano ferrite; structural; sol–gel auto-combustion; impedance study; magnetic study

1. Introduction

Ferrites are magnetic materials that have been extensively researched. However, there is a growing interest in studying the magnetic, electric, and structural properties of mixed spinel ferrites due to the numerous potential applications and the need to comprehend the physical processes involved in order to improve these materials for different technological applications. Magnetic, electric, and structural properties are affected by the crystallite size, sintering temperature, and ionic distribution among sites, among many reasons [1–5]. Due to its widespread applications in medication delivery, high-density information storage, ferrofluids, and other technical areas, ferrite materials are gaining increasing attention [3,5]. Spinel ferrites have a general formula AFe_2O_4, where A denotes the divalent metal ion (e.g., Zn, Mn, and Ni). Furthermore, researchers in the field of magnetism, electronics, and biotechnology have increasingly explored a category of materials called "spinel ferrites" because of their potential applications in wastewater treatment, high-density storage, spin-dependent electrical devices, and medicinal therapy [3–6].

Magneto mechanical, magneto-optical, noncontact torque sensing, magnetic stress sensors, and high magnetostriction applications are desirable for manganese-doped cobalt ferrites [7–8]. The magnetic behavior of spinel ferrites is caused by the difference in the magnetic moment of the distributed cations in the tetrahedral (A-site) and octahedral (B-site) sites. Furthermore, the super-exchange interactions A–O–B, A–O–A, and B–O–B play measured roles, with A–O–B being the strongest interaction [9].

Among all the spinel ferrites, cobalt ferrite ($CoFe_2O_4$, CFO) has caught researchers' attention due to its tunable magnetic and dielectric properties, as well as its potential applications in manufacturing memory, capacitors, filters, and microwave devices [5]. CFO has an inverse spinel structure with two interstitial sites called the tetrahedral site (A-site) and octahedral site (B-site), in which Fe^{3+} ions occupy the tetrahedral site, while both the Fe^{3+} and Co^{2+} occupy the octahedral site in equal amounts. CFO forms the FCC crystal lattice structure with 56 ions per unit cell, in which the larger number of oxygen ions is arranged in the dense FCC structure and the smaller number of cobalt ions occupies the space between them. CFO has moderate saturation magnetization, remarkable mechanical hardness, and strong magneto crystalline anisotropy constant value, which makes it technologically important [3].

Generally, the compound having an inverse spinel structure facilitates the doping of various transition metals to enhance its structural, magnetic, and dielectric properties. Thus,

---

✉ Corresponding author: Sunirmal Saha E-mail: sunirmal.saha@cgu-odisha.ac.in, slrsixsept@gmail.com

Springer

past research efforts were directed at substituting divalent metal ions, such as Mg^{2+}, Bi^{2+}, Ni^{2+}, and Mn^{2+}, in CFO for the application prospect, mostly in high-frequency device applications [10–11]. Studies have also shown that doping CFO with Ni enhances its magnetic properties due to the smaller ionic radius of Ni^{2+} compared to Co^{2+}, thus leading to increased saturation magnetic (M_s) and residual magnetization (M_r) [12]. For instance, Ni-doped CFO often exhibits a higher M_s value than pure CFO, as the substitution improves magnetic ordering. Cu doping has been reported to reduce the M_s value, similar to Mn doping [13]. The incorporation of Cu, which has a lower magnetic moment, can lead to the dilution of the overall magnetic properties. Studies indicate that Cu-doped CFO shows a decrease in magnetization with increased Cu concentration due to the suppression of super-exchange interactions [14]. Zn-doped CFO typically results in lower magnetic properties due to the nonmagnetic nature of Zn^{2+}. This effect is similar to what has been observed with Mn doping, in which the overall magnetic moment decreases as more nonmagnetic ions are introduced into the lattice [15]. In contrast to other dopants, Mn^{2+} doping in CFO has been shown to enhance residual magnetization (M_r) from 37.77 to 51.89 emu/g, suggesting that Mn interaction with the lattice creates favorable conditions for maintaining magnetic order [16]. When Mn^{2+} is substituted, the properties of CFO will become advantageous for applications based on high magneto-dielectric (MD) responses.

The synthesis route highly influences the properties of the CFO and its substituted system. Consequently, several methods have been studied to achieve synthesis, including sol–gel auto-combustion, solid-state reaction, solvothermal method, etc., among which sol–gel auto-combustion has the benefits of low cost, availability, reasonable stoichiometric control, and high purity [17]. For these reasons, we considered sol–gel auto-combustion in the current study to synthesize nanoparticles. Based on our previously reported works on synthesis techniques of transition metal-doped CFO, the sol–gel auto-combustion technique does not require any equipment to yield ultrafine nanoparticles [18–21]. Thus, this specific technique was used in the present study to synthesize the nanoparticles of a $CoMn_xFe_{(2-x)}O_4$ (x = 0.00, 0.05, 0.10, 0.15, 0.20) system (MCFO). The impacts of the annealing and evaporation on the structural, magnetic, and dielectric properties were also analyzed.

The main objective of this study was to add Mn^{2+} to CFO through the sol–gel auto-combustion route varying from 0.00 to 0.20wt%. The cation distributions at the tetrahedral and octahedral sites of the material have an impact on the structural and magnetic properties. Furthermore, the MD property, along with the dielectric property, was emphasized. A thorough literature review showed that including Mn^{2+} in CFO leads to good dielectric and magnetic properties. Many researchers have investigated the impacts of substituting Mn^{2+} at the Co^{2+} site on the structural, magnetic, and dielectric characteristics. Still, there is insufficient research on adding Mn^{2+} at the Fe^{3+} site. In addition, the oxidation states of Mn^{2+} and Fe^{3+} differ, so studying the changes and interpreting the analysis could also be interesting. As such, in order to study the structural, magnetic, and MD properties of the CFO-substituted Mn at the Fe^{3+} site, this study conducted crystal structure, magnetic property, and MD analyses.

2. Experimental

The stoichiometric quantities of manganese nitrate ($Mn(NO_3)_2\cdot 4H_2O$), cobalt nitrate ($Co(NO_3)_2\cdot 6H_2O$), iron nitrate ($Fe(NO_3)_3\cdot 9H_2O$) and glycine, all from Merck Co., India, with a minimum purity of 99%, were used without additional purification. Then, these were dissolved in distilled water and stirred to form a homogenous clear solution. Without the protection of inert gases, the reaction method was carried out in atmospheric air. The solution was heated at 150°C for 7–8 h while constantly stirring on a hot plate magneto-stirrer. As the solution thickened, it eventually formed a brownish gel due to the ongoing water evaporation. The resulting gels were continuously heated for 3–4 h at 210°C. The sticky mass started to bubble, and the gel automatically caught fire with bright flints once the leftover water was removed from the mixture. A puffy solid remained after self-propagating combustion occurred, taking less than 1 min to complete. The puffy solid was then ground to a powder before being used for characterization. This solid was further milled for 30 min after being calcined at 600°C for 3 h at a heating rate of 5°C/min to remove any organic material that may have been present in the system. The synthesis process is shown in Fig. 1.

3. Results and discussion

3.1. XRD analysis

Fig. 2 depicts information regarding phase identification and structural parameters from X-ray diffraction (XRD) characterization. This process was carried out in the angle range of 20°–70° at room temperature (RT). The XRD pattern of all the as-synthesized MCFO samples (Fig. 2) matches the ICDD database No. 22-1086, thus signifying the presence of the spinel structure and an $Fd\bar{3}m$ space group. In accordance with the ICDD database, specific major diffraction peaks are present, and no significant change occurred after the Mn^{2+}doping [7]. A slight shift of the XRD peaks to higher 2θ values can be seen, which is attributable to lattice contraction resulting from the substitution of Mn^{2+} for Fe^{3+} ions. Given that the ionic radius of Mn^{2+} (0.83 Å) is smaller greater than that of Fe^{3+} (0.64 Å) in the octahedral sites, replacing Fe^{3+} with Mn^{2+} reduces the lattice parameters, which is reflected as a shift toward the higher 2θ values in the XRD pattern. The observed shift in the XRD pattern of the (311) diffraction peak with increasing Mn doping can be attributed to several interrelated factors. First, the ionic radius of Mn^{2+} (0.83 Å) is smaller than that of Co^{2+} (0.87 Å) and Fe^{3+} (0.64 Å). When Mn is incorporated into the crystal lattice of the material, the smaller size of Mn ions leads to a contraction of

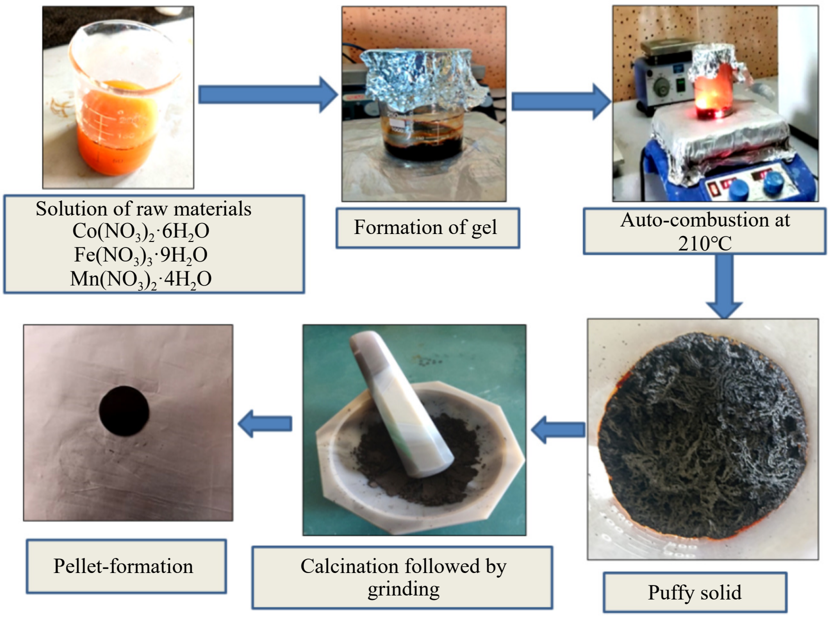

Fig. 1. Schematic of different stages of the sol–gel process.

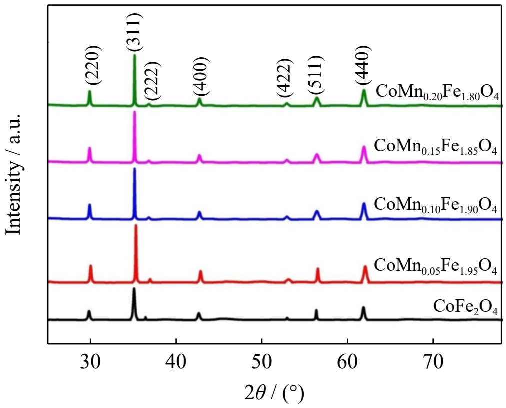

Fig. 2. XRD patterns of $CoMn_xFe_{(2-x)}O_4$ samples.

the lattice parameters initially, which is reflected in a shift of the diffraction peak to a higher angle according to Braggs law. Furthermore, the incorporation of Mn can create local lattice distortions and strain, particularly if there is a significant difference in the concentration of dopants or if they are substituted for larger cations. These strains can affect the interatomic distances, resulting in altered diffraction patterns. As the doping concentration of Mn increases, the initial shift to a higher angle may indicate the dominance of Mn incorporation, leading to a tighter packing of the lattice. However, at higher concentrations, the lattice may begin to experience further strain or even a transition to different crystal phase or structure due to the interactions between the dopant ions. This can cause a subsequent shift of the peak to a lower angle as the lattice expands due to these factors. At higher doping levels, there might be a transition from one crystal structure to another or the formation of secondary phases, which can further contribute to shifts in the diffraction peaks. These changes may alter the overall symmetry and dimensions of the crystal lattice, leading to the observed behavior in the XRD pattern. Furthermore, (311) is the most substantial reflection peak, and we calculated its particle size using the Scherrer formula. The XRD spectra broadening is observed as the particle size is on a nanoscale. The lattice parameter (a), X-ray density (ρ_x), and crystallite size (D) are calculated using the formula below [22]:

$$a = d\left(h^2 + k^2 + l^2\right)^{1/2} \tag{1}$$

$$\rho_x = \frac{8M}{Na^3} \tag{2}$$

$$D = \frac{0.9\lambda}{\beta\cos\theta} \tag{3}$$

where d is the inter-planner spacing, M is molecular weight, h, k, l are the miller indices plane, λ is the wavelength of X-ray, β is full-width half-maxima, N represents Avogadro's number, which is 6.022×10^{23} mol^{-1}, and D is the crystallite size. The structural parameters, such as crystallite size, X-ray density, lattice parameter, and d-spacing, are tabulated in Table 1. As can be seen, the lattice parameter (a) increases after the Mn doping increases. This may be due to the larger ionic radius of Mn^{2+} (0.83 Å) compared to Fe^{3+} (0.64 Å) [23]. The values of the average crystallite size (D) of the prepared samples are in the nanometer range. Furthermore, the X-ray density value decreases linearly when the incorporation of doping concentration increases due to the light weight of Mn compared to Fe.

3.2. Field emission scanning electron microscopy (FESEM) analysis

Fig. 3 illustrates the FESEM images of the as-synthesized MCFO series. As can be seen, the particles are highly aggregated due to the surface reaction and magnetic properties of CFO. Doping Mn^{2+} into CFO nanoparticles influences the shape, uniformity, grain morphology, and homogeneity [24]. Furthermore, particle size continuously decreases when the Mn concentration increases, indicating that Mn substitution restricts crystal growth. The substitution with strong site preference also reduces the particle size as the substitution

Table 1. Various structural parameters of $CoMn_xFe_{(2-x)}O_4$ (x = 0, 0.05, 0.10, 0.15, 0.20) nanoferrite particles

Composition	Lattice parameter / Å	Volume of unit cell, a^3 / cm^3	Crystalite size, D / nm	2θ of (311) peak / (°)	d-spacing / Å	Full width at half maximum
$CoFe_2O_4$	8.312	574.27	55.20	35.48	3.21	0.1222
$CoMn_{0.05}Fe_{1.95}O_4$	8.308	588.69	46.42	36.39	2.46	0.2880
$CoMn_{0.10}Fe_{1.90}O_4$	8.311	591.01	42.33	36.23	2.47	0.3456
$CoMn_{0.15}Fe_{1.85}O_4$	8.293	591.22	36.38	36.34	2.46	0.4032
$CoMn_{0.20}Fe_{1.80}O_4$	8.286	593.97	31.40	36.19	2.48	0.3457

ion increases. The release of high amounts of gases in the auto-combustion process contributes to the porous structure obtained from Fig. 3. Some regions in the FESEM images seem to be agglomerated. The main reason is the interaction between the calcination temperature and magnetic behavior, and the fact that spinel ferrite nanoparticles tend to get agglomerated. As shown in Fig. 3(a), pure CFO nanoparticles have the largest grain distributed non-uniformly compared to other micrographs. All of these results from FESEM images are in good agreement with XRD findings.

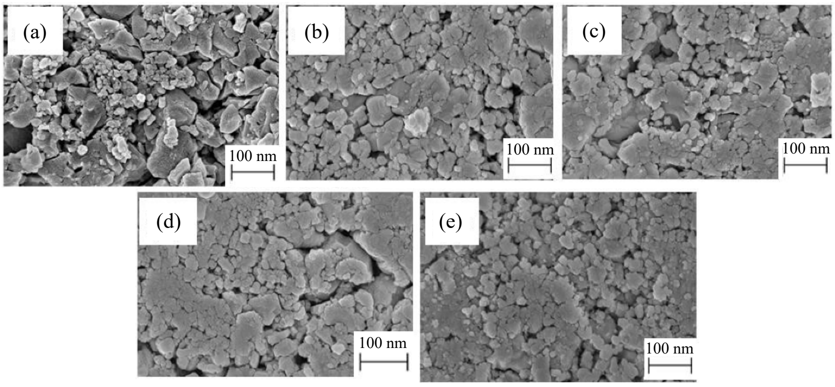

Fig. 3. FESEM images of the $CoMn_xFe_{(2-x)}O_4$ nanoparticle: (a) $x = 0$; (b) $x = 0.05$; (c) $x = 0.10$; (d) $x = 0.15$; (e) $x = 0.20$.

3.3. X-ray photoelectron spectroscopy (XPS) analysis

XPS analysis was performed to investigate the material's surface chemical composition and oxidation state. In XPS, the surface chemistry of the material, known as the photoelectric effect, can be studied by analyzing the energies of the emitted electrons. The XPS spectra of the MCFO sample are illustrated in Fig. 4. It gives valuable ideas on the surface chemistry of chemicals present. The survey scan of the MCFO series of the sample is shown in Fig. 4. All the samples exhibit the Co 2p, Fe 2p, O 1s, and C 1s peaks, with no significant differences observed in their full scan XPS spectra. The C 1s spectrum was used as a reference for charge correction. In the high-resolution XPS spectrum of Co 2p, the Co $2p_{3/2}$ and Co $2p_{1/2}$ binding energy (B.E.) peaks are observed at 781.3 and 798.3 eV, respectively. Satellite features at 785.8 and 811.3 eV confirm the presence of Co^{2+} oxidation state [25]. The Co 2p spectrum shows Co $2p_{3/2}$ and Co $2p_{1/2}$ peaks at 983.1 and 963.8 eV, respectively, along with a satellite peak at 938.5 eV, which is characteristic of Co^{2+} [26]. The high-resolution XPS spectrum of Fe 2p displays Fe $2p_{3/2}$ and Fe $2p_{1/2}$ peaks at 713.8 and 735.7 eV, respectively.

Additionally, the Fe $2p_{3/2}$ peak at 713.6 eV indicates the presence of Fe^{3+} at the tetrahedral sites, and the satellite feature located at 729.3 eV further confirms the Fe^{3+} oxidation state. The high-resolution XPS spectrum of O 1s exhibits peaks at 531.2 and 542.4 eV, corresponding to lattice oxygen and oxygen defects, respectively [25]. These XPS results verify the presence of the elements in their respective oxidation states. The XPS data further confirm that Mn is successfully incorporated into the CFO nanoparticles, in agreement with the XRD results. The XPS signals of Co 2p, Fe 2p, and Mn 2p are presented in Fig. 4(b)–(d) of the composition $CoMn_{0.20}Fe_{1.80}O_4$, thus verifying the existence of Co, Fe, and Mn in the composition. The high-resolution XPS spectrum of Co 2p is presented in Fig. 4(b), which shows two spin-orbit doublet characteristics with two satellite peaks.The satellite peak and binding energy corresponding to Co $2p_{3/2}$ are at 783.7 and 777.2 eV, respectively, and along with it, the satellite peaks of Co $2p_{1/2}$ are at 793.0 and 800.0 eV, which are associated with the binding energy [25]. The XPS spectra after the Mn^{2+} doping have an impact on the crystal structure and the binding energy of the pure CFO. Two peaks are found by fitting the high-resolution spectra of Fe 2p. In Fig. 4(c), we can see that at 709 and 721.8 eV, there are two prominent peaks of Fe^{2+}, which describe its presence. Furthermore, the significant peaks for Mn^{2+}, corresponding to Mn $2p_{3/2}$ and Mn $2p_{1/2}$, are at 639.8 and 651.5 eV, respectively, as shown in Fig. 4(d) [26].

3.4. Raman spectra

Fig. 5, which illustrates a little spectral shift, represents the RT Raman spectra of the MCFO series samples in the frequency ranging from 200 to 1000 cm^{-1}. This shift is determined by bond length and strength, which in turn, are influenced by dopant concentrations. When the Mn content increases, the peaks become broader. As CFO has an inverse

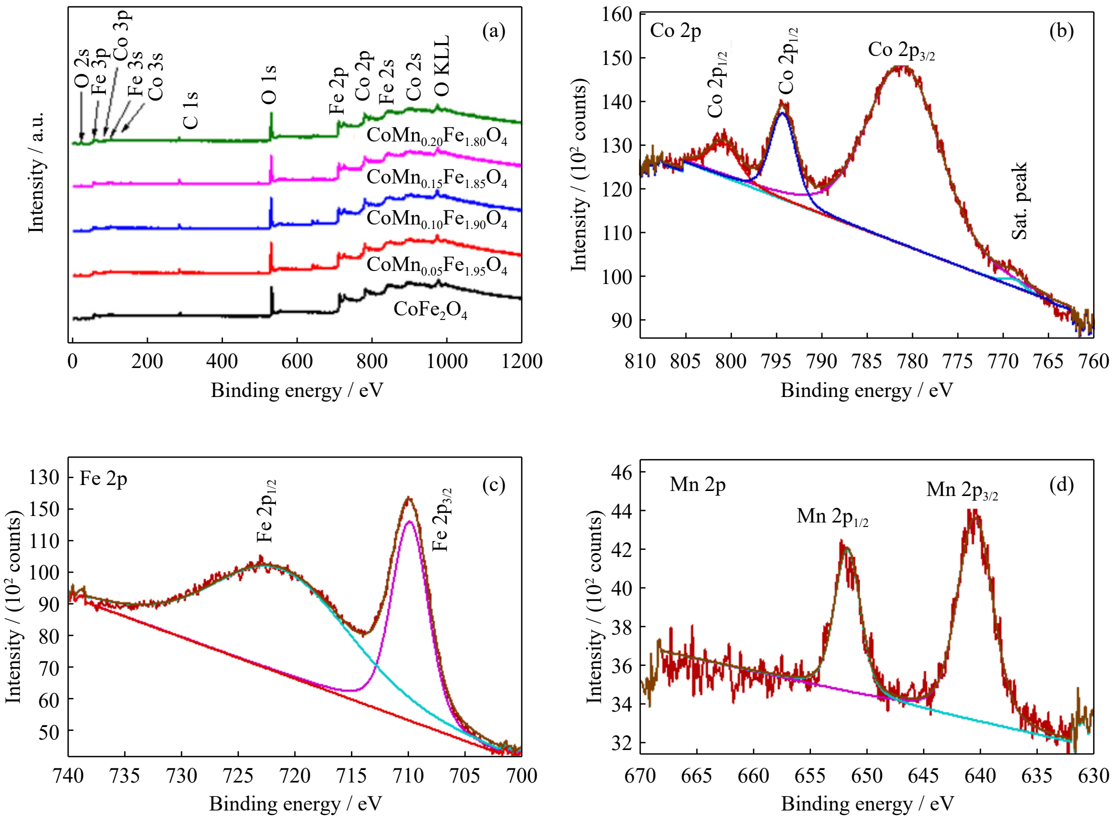

Fig. 4. XPS spectra of (a) MCFO series samples and convoluted XPS spectra for $CoMn_{0.20}Fe_{1.80}O_4$ of (b) Co 2p, (c) Fe 2p, and (d) Mn 2p.

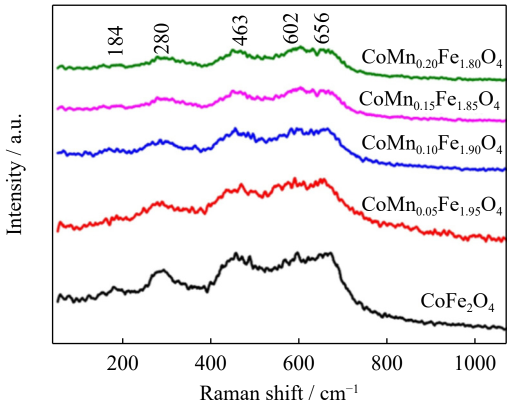

Fig. 5. Raman spectra of $CoMn_xFe_{(2-x)}O_4$ series samples.

spinel structure, it is worth mentioning that the tetrahedral site occupies half of the Fe^{3+} cation. In comparison, the remaining half of the Fe^{3+} and Co^{2+} cations are distributed throughout the octahedral site. This structure has five optically Raman active modes: A_{1g}, E_g, and $3T_{2g}$. There are three major bands observed at 280, 463, and 656 cm^{-1}, respectively. Furthermore, bands at 184 and 602 cm^{-1} are minor bands as these are comparatively less intense [27]. The occurrence of these peaks in the Raman spectra is due to the symmetric stretching of the metal–oxygen bond. The E_g and T_{2g} modes occur through the asymmetrical vibration of metal–oxygen at the octahedral site, while the A_{1g} mode is connected with the symmetric stretching of oxygen atoms along the metal–oxygen bond in the tetrahedral coordination. In the spinel structure with the $Fd\bar{3}m$ space group, 39 normal modes are assigned [28] as follows: $\Gamma = A_{1g} + E_g + F_{1g} + 3F_{2g} + A_{2u} + 2E_u + 4F_{1u} + 2F_{2u}$, among which four are infrared active and five are Raman active modes.

The high-frequency modes (above 600 cm^{-1}) arise due to the vibration in the tetrahedral site, while the low-frequency modes (400 cm^{-1}) are related to the octahedral site. The peak broadening due to Mn^{2+} doping can be attributed to the local disorderedness in CFO. The migration breaks the long-range cation order, creating disorder in the site's tetrahedral and octahedral sublattices. This phenomenon is due to the Fe^{3+} ions present in the tetrahedral site moving from the tetrahedral to the octahedral site, while the Co^{2+} ions simultaneously migrate from the octahedral to the tetrahedral site. During the migration between both sites, the divalent and trivalent cation distribution changes, leading to the disorderedness influenced by the Mn^{2+} ion. All five peaks, found in 184, 280, 463, 602, and 656 cm^{-1}, correspond to the Raman active modes $T_{2g}(1)$, E_g, $T_{2g}(2)$, $T_{2g}(3)$, and A_{1g} which confirms the spinel structure of the MCFO samples. However, in the bulk form of CFO, these peaks are located in different positions due to the difference in the distribution of cations in these two sites [28].

3.5. Magnetic properties (vibrating sample magnetometer-VSM study)

VSM was used to analyze the RT magnetic properties of MCFO in the magnetic field of $-20\ \text{kOe} \le H \le 20\ \text{kOe}$.

Fig. 6 presents the magnetic hysteresis (M–H) loop. The saturation magnetization (M_s), coercivity (H_c), Bohr magneton (η_B), retentivity (M_r), squareness ratio (M_r/M_s), and anisotropy constant (K) values were calculated, and shown in Table 2. The hysteresis loop reveals the ferromagnetic nature of all the samples, which can be explained by Neel's model. Based on Neel's sublattice model, A–B super-exchange interaction is more effective than A–A and B–B interactions, and this model also describes the cation distribution between tetrahedral and octahedral sites [29]. The total magnetization in the spinel ferrite is the difference between the magnetic moment of the A- and B-site.

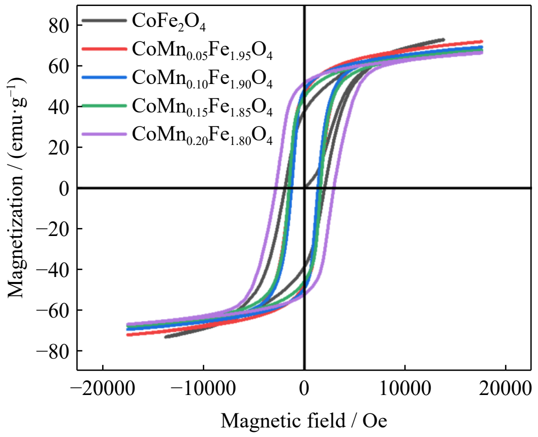

Fig. 6. Hysteresis loop for the $CoMn_xFe_{(2-x)}O_4$ series samples at room temperature.

Fig. 6 shows that M_s decreases with increasing Mn^{2+} substitution. For $x = 0.20$, the M_s value is the lowest due to the disturbance in the Fe–O–Fe interaction. When Mn is incorporated into CFO, the Fe^{3+} density decreases at the octahedral site with the rise in Mn^{2+} concentration, thus reducing the total magnetic moment of the sublattice. The magnetic properties of the CFO and its modified system depend upon the cation distribution among the tetrahedral and octahedral sites, as well as particle size. After adding Mn^{2+}, the particle size decreases, leading to the M_s decreases. The H_c value is reduced initially after the Mn substitution in the CFO nanosystem [30]. This decrease in H_c is due to the reduced magnetization energy barrier after the Mn^{2+} substitution. We also compared the magnetic moment of Mn ($3\eta_B$) to Fe ($5\eta_B$). The magnetic moment per formula unit was estimated in terms of Bohr magnetons applying the following formula [30]:

$$\eta_B = \frac{M \times M_s}{5585} \tag{4}$$

where M is the molecular weight of the sample.

The K value can be determined based on the Stoner–Wohlfarth model using the values of M_s and H_c [31–32] as follows:

$$K = \frac{H_c \times M_s}{0.98} \tag{5}$$

From Table 2, the M_r value increases with the increasing wt% of Mn into CFO. M_r is the magnetization that remains in the ferromagnetic material after the magnetic field has been withdrawn. This phenomenon is called residual magnetization. M_r values range from 37.77 to 51.89 emu/g. The amount of energy required to spin the magnetic moment beyond the axis of magnetization is called the "anisotropy constant" (K) [33–34]. The Bohr magneton or the magnetic moment per unit decreases from $3.07\eta_B$ to $2.80\eta_B$. This is another reason for decreasing M_s after the incorporation of Mn^{2+} in the CFO.

3.6. Dielectric analysis

The dielectric constant (ε') and dielectric loss factor (ε'') were analyzed by using an LCR meter in the frequency range of 100 Hz–1 MHz with varying temperatures from RT to 400°C. The dielectric property of the sample has been explained by Koop's theory, the Maxwell–Wagner polarization process and the hopping mechanism of the electrons [35]. The dielectric properties of a material depend on the synthesis route, chemical composition, particle size, and porosity, among many factors. The following formula is used for the dielectric constant calculation [36]:

$$\varepsilon' = \frac{Cd}{\varepsilon_0 A} \tag{6}$$

where A represents the area of the pellet in m^2, C is the capacitance of the pellet in F, d denotes the thickness of the pellet in m, and ε_0 represents the permittivity of the free space. Fig. 7(a) shows the dielectric response graph of the synthesized material MCFO.

From Fig. 7(a), when the frequency increases, the ε' value decreases to a certain level, then maintains a constant value. Furthermore, the decrease in the ε' is very sharp in the lower frequency range compared to the high-frequency range [37]. This result shows a simultaneous effect of different polarizations taking place at lower frequencies, thus developing a high dielectric constant value, which in turn, decreases at high frequencies due to the decreasing contribution. This result also provides us with information related to the electrical conduction mechanism, which is the dielectric response of the applied electric field. The normal dielectric behavior of the Mn^{2+}-substituted CFO is due to polarization, and the conduction mechanism leads to the polarization between Fe^{2+}

Table 2. Magnetic parameters obtained at the 0–20 kOe magnetic field

Sample	M_s / (emu·g^{-1})	H_c / Oe	Retentivity, M_r / (emu·g^{-1})	Squareness ratio, R (M_r/M_s)	η_B	K / (10^4 erg·cm^{-3})
$CoFe_2O_4$	73.12	1939	37.77	0.52	3.07	14.46
$CoMn_{0.05}Fe_{1.95}O_4$	72.13	1499	47.19	0.65	3.02	11.03
$CoMn_{0.10}Fe_{1.90}O_4$	69.41	1312	48.63	0.70	2.91	9.30
$CoMn_{0.15}Fe_{1.85}O_4$	67.87	1562	45.20	0.66	2.85	10.81
$CoMn_{0.20}Fe_{1.80}O_4$	66.84	2875	51.89	0.78	2.80	19.60

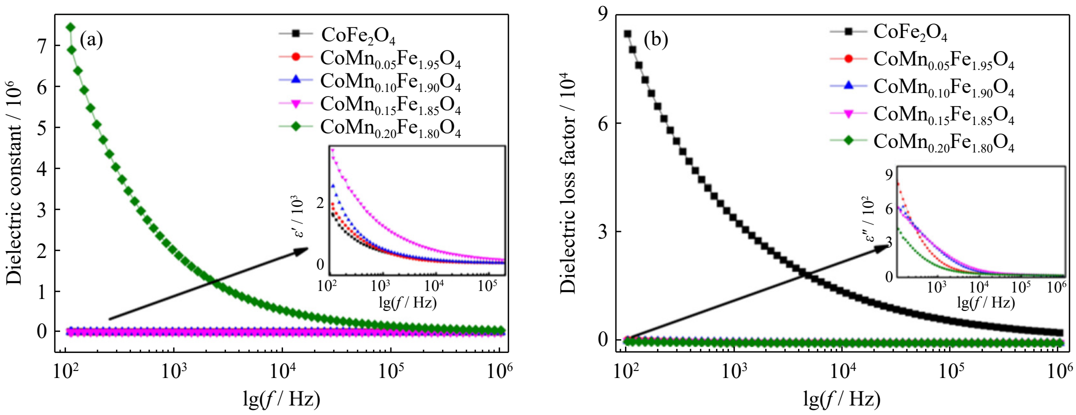

Fig. 7. Frequency-dependent dielectric plots of $CoMn_xFe_{(2-x)}O_4$ samples at room temperature: (a) dielectric constant (ε′); (b) dielectric loss factor (ε″).

and Fe^{3+} ions. The dielectric constant value is high in the lower frequency region due to the space charge polarization. We noticed that at high frequency, the ε′ value of all the synthesized material is saturated, which can be ascribed to the Maxwell–Wagner interfacial theory [38]. This theory posits that polarization occurs in the material, formed by well-conducting grains separated by nonconducting grain boundaries. After a particular frequency, the hopping of electrons cannot follow the alternating current, thus slowing down the exchange. As a result, the polarization also tends to decrease and maintains a steady state at higher frequencies. When the concentration of Mn doping is increased, the ε′ value is increased due to a decrease of the hopping mechanism at the grain boundary to which the charge accumulation at the grain boundaries increases. The increase in ε′ value with increasing Mn concentration agrees with the previously reported results [39–40].

Fig. 7(b) shows the dielectric loss factor (ε″) vs. frequency ranging from 100 Hz to 1 MHz. Dielectric loss refers to the energy loss of the dielectric material and is related to dispersion, which occurs when polarization slows down the applied electric field due to the grain boundaries and imperfections in the crystal lattice. The hopping of the charge carriers increases in the octahedral site when the frequency is high due to the active grains, so the dielectric loss is saturated at high frequency. The space charge, orientation, electronic polarization, and grain boundary effect mainly impact the energy dissipation at lower frequencies [41]. As the resistivity is high at the grain boundary, the dielectric loss value is high at lower frequencies, while it requires high energy for the electron exchange in low frequencies. The dielectric loss value is independent at high frequencies and can be explained by Koop's theory and the Maxwell–Wagner model [38].

Fig. 8 presents the frequency vs. ε′ in the temperature ranging from RT to 400°C for the synthesized MCFO series of samples. For all temperatures, ε′ is reduced consistently with increasing frequency, which is the normal typical behavior of dielectric materials [41]. This result is due to the decrease in

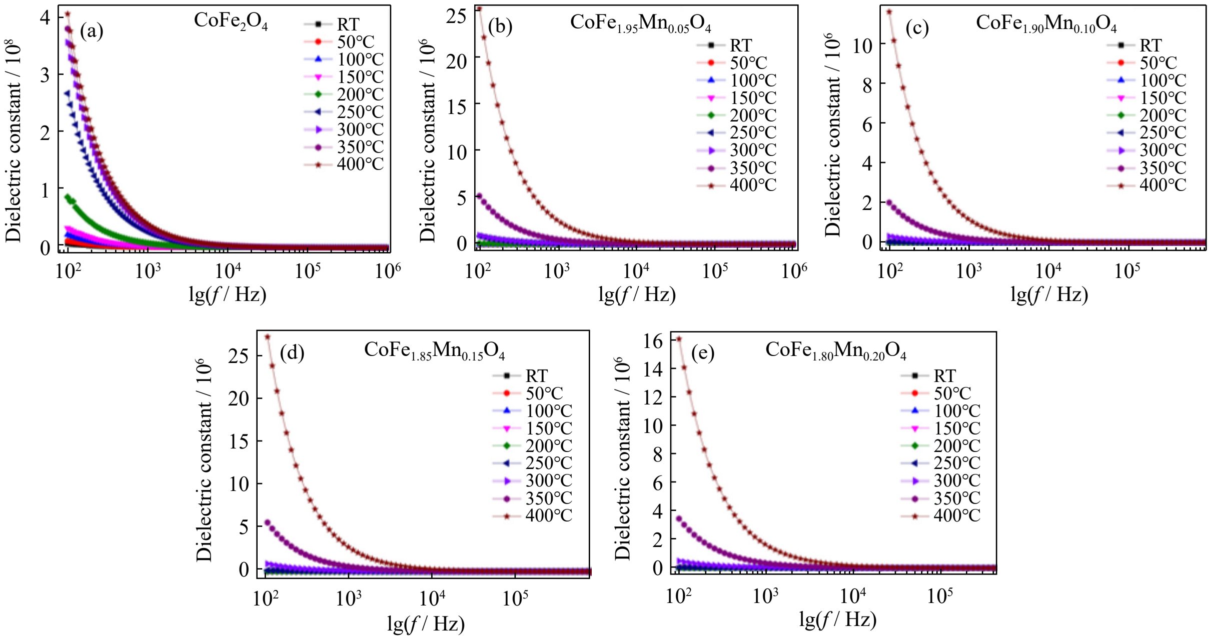

Fig. 8. Variation of dielectric constant (ε′) with frequencies for $CoMn_xFe_{(2-x)}O_4$ samples at different temperature: (a) $x = 0$; (b) $x = 0.05$; (c) $x = 0.10$; (d) $x = 0.15$; (e) $x = 0.20$.

the space charge polarization. As the ε' increases with an increase in temperature, after a particular frequency, it becomes constant. At low temperatures, charge carriers have limited mobility, resulting in weak polarization and a lower ε'. As the temperature increases, thermal agitation frees more bound charge carriers, thus increasing their mobility and contributing to polarization. This, in turn, results in an increase in the ε' value. The observed increase in ε' with increasing temperature and decreasing frequency aligns with the Maxwell–Wagner theory, which explains dielectric dispersion in heterogeneous systems, and Koop's phenomenon, which describes the frequency dependence of the dielectric constant that is consistent with our observation. In the Mn^{2+}-substituted ferrite samples, ε' increases with temperatures of up to 400°C. The substitution of Mn in CFO impacts these lattice dynamics, thus influencing the dielectric properties.

3.7. Electrical properties

3.7.1. AC conductivity

The frequency-dependent AC conductivity (σ_{ac}) was investigated to better explain the charge transport mechanism. Fig. 9 illustrates the variation of AC conductivity with a frequency range of 100 Hz–1 MHz within the temperature ranging from RT to 400°C for the MCFO series of the sample. Spinel ferrites generally exhibit an increase in AC conductivity as temperatures increase. The value of σ_{total} at a particular temperature describes Jonscher's universal dielectric response (UDR) law. Following the UDR law, the total conductivity (σ_{total}) can be represented as follows [42]:

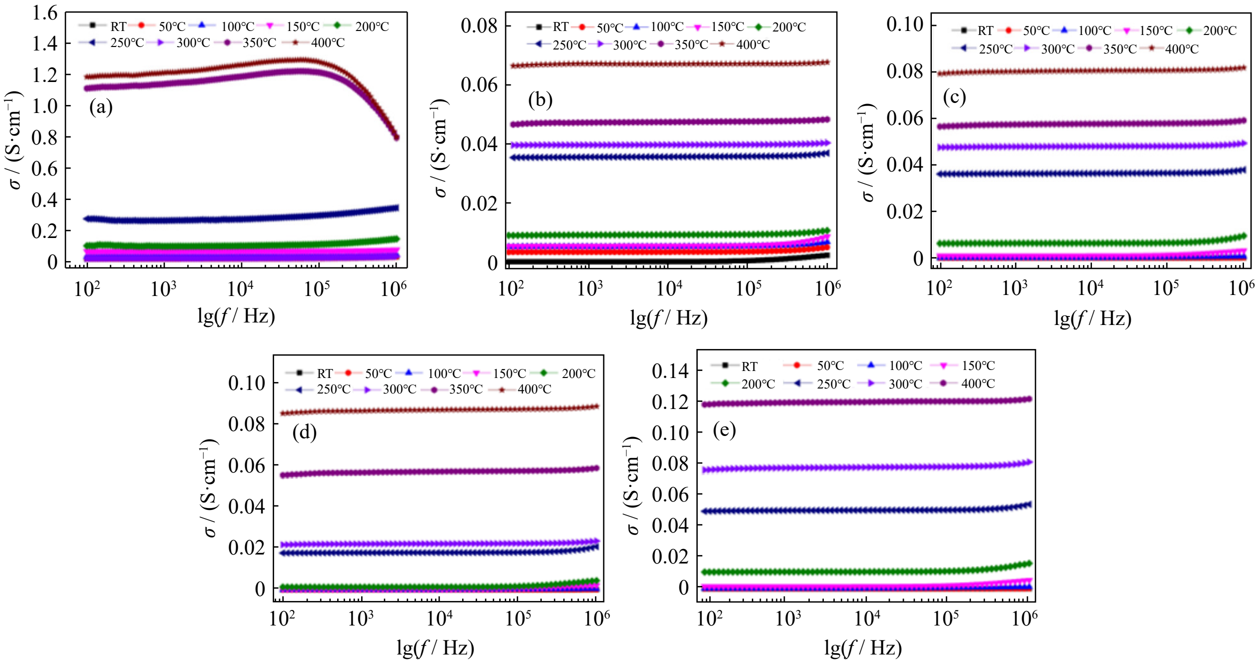

Fig. 9. Variation of AC conductivity (σ_{ac}) with frequencies for $CoMn_xFe_{(2-x)}O_4$ samples at different temperatue: (a) x = 0; (b) x = 0.05; (c) x = 0.10; (d) x = 0.15; (e) x = 0.20.

$$\sigma_{total} = \sigma_{dc} + \sigma_{ac} \tag{7}$$

where σ_{dc} is DC conductivity, and σ_{ac} is the frequency-dependent AC conductivity. The AC conductivity based on Eq. (7) contains two terms: the frequency-independent term σ_{dc} and the frequency-dependent term σ_{ac}. However, across the entire frequency range investigated, the AC conductivity data appear to be almost independent of frequency. The expected frequency dependence of AC conductivity is typically observed in materials where hopping conduction mechanisms or relaxation processes are significant. However, in our study, the absence of noticeable frequency dependence in the AC conductivity data suggests that the frequency-independent term σ_{dc} might be dominating the AC conductivity over the entire frequency range under investigation. This occurrence is due to the DC conductivity component, which is much larger compared to the frequency-dependent component, leading to a nearly constant overall conductivity. Furthermore, the frequency range in our investigation might not be wide enough to observe significant changes in the frequency-dependent term σ_{ac}. The charge carriers are primarily mobile ions or electrons with low hopping activation energy; therefore, the AC conductivity might remain constant over a broad frequency range.

3.7.2. Impedance analysis

Impedance analysis is an effective method for understanding the electrical characteristics of ferrite nanoparticles. Given that ferrites are polycrystalline materials, the inter-grain boundaries are inadequate areas where oxygen stoichiometry might deviate, and dopants, contaminants, or subsequent phases can separate. The complex impedance (Z^*) can be defined as

$$Z^* = Z' + jZ'' \tag{8}$$

where Z' is the real part of the impedance, and Z'' is the imaginary part of the impedance. This equation describes the resistive and reactive contributions when the AC field is applied [43]. The resistive phase is symbolized by the real part Z', whereas the reactive component is expressed by Z''.

Figs. 10 and 11 show the variation of the real and imaginary impedance spectra, respectively, of the parent and Mn-substituted nano CFO in the frequency range 100 Hz–1 MHz and temperature range of RT to 400°C. As shown in the plot, the Z' value decreases continuously up to a certain frequency range, after which it remains constant and merges together. The relaxation process in Z' is caused by the conduction of space charges. Due to the increased temperature, the thermal energy is enhanced, allowing the space charges to follow a higher frequency [44]. As shown in Fig. 10, the substitution of Mn in the CFO system has efficiently reduced the space charge conduction.

Fig. 11 depicts the imaginary part of impedance vs. frequency plot of CFO series samples at different temperatue. This represents that the Z'' value is reduced with the increasing frequency, but after reaching a certain limit, it becomes frequency-independent. Two prominent peaks are observed

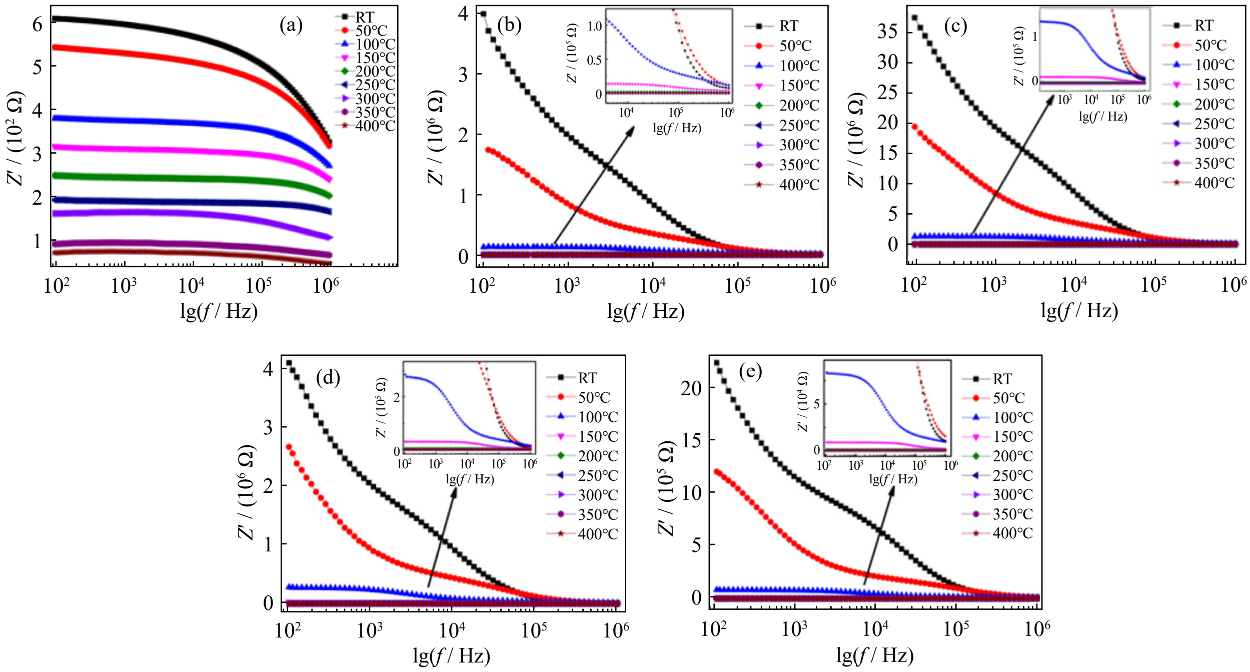

Fig. 10. Variation of the real part of impedance (Z') with frequencies for $CoMn_xFe_{(2-x)}O_4$ samples at different temperature: (a) $x = 0$; (b) $x = 0.05$; (c) $x = 0.10$; (d) $x = 0.15$; (e) $x = 0.20$.

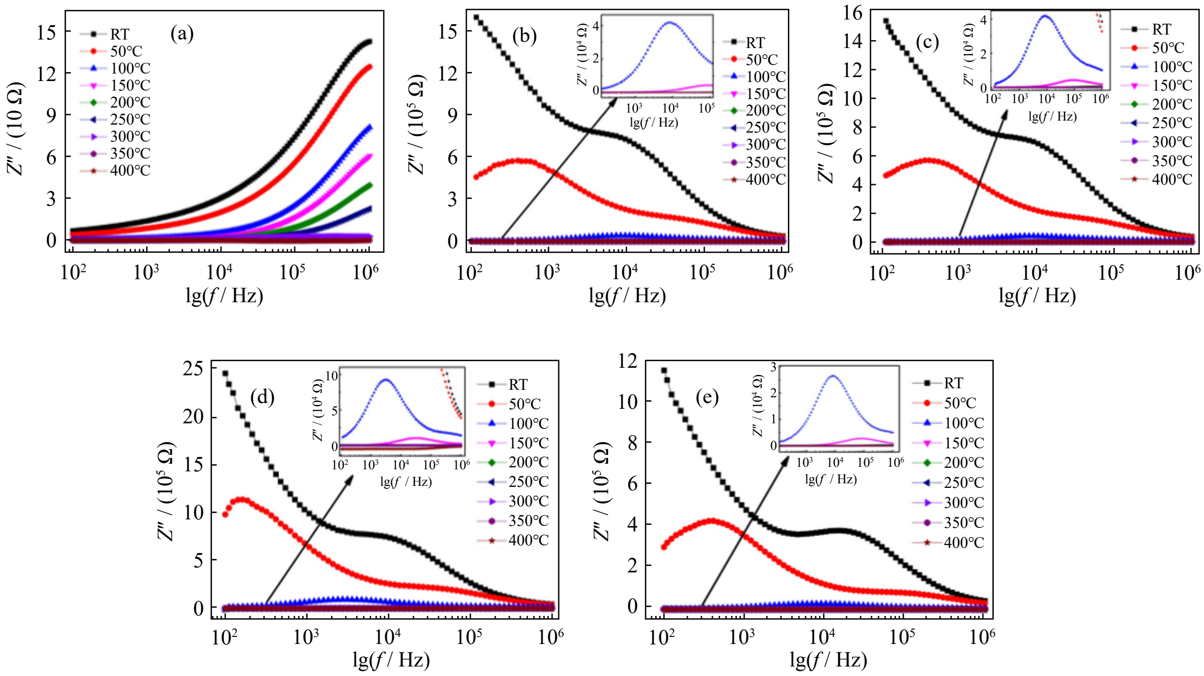

Fig. 11. Variation of the imaginary part of impedance (Z'') with frequencies for $CoMn_xFe_{(2-x)}O_4$ samples at different temperature: (a) $x = 0$; (b) $x = 0.05$; (c) $x = 0.10$; (d) $x = 0.15$; (e) $x = 0.20$.

at the low temperature in the MCFO series of the samples, and when the temperature increases, the width of the peak decreases and shifts to the higher frequency region. As the electrical behavior is frequency dependent, the relaxation peaks imply the presence of space charge. When the Z'' value drops, the temperature and frequency both increase. The relaxation peak is due to the grain boundary [38].

Furthermore, the value of Z' and Z'' decreases with increasing frequency, implying the relaxation behavior is temperature dependent. The combined graph between the imaginary part of the impedance and electric modulus to frequency is presented in Fig. 12. This was analyzed in RT within a frequency range of 100 Hz–1 MHz. As shown in Fig. 12, two relaxation peaks that arise at RT in pristine CFO. Nevertheless, adding manganese suppresses the relaxation peak occurring at the lower frequency region, and the extent of suppression of the peak rises as the manganese concentration increases.

The relaxation peak at a lower frequency of the Z'' spectrum is caused by the charge carriers' conduction in the region with the highest capacitive domain, which has been explained as a response to the electrode surface contact effect [39]. Additionally, the imaginary part of the modulus (M'') was inversely related to capacitance. The results show that the conduction effect at the highest capacitive region is suppressed by it. Some reports have revealed the absence of the grain effect and the dominance of the interfacial conduction mechanism. In the graph, the gap among the maximum peak position of Z'' and M'' increases as the manganese concentration increases, thus indicating the promotion of charge carrier-localized motion and showing the comparatively more non-Debye conduction type when taken in RT [40]. Furthermore, including Mn^{2+} in CFO increases the potential barrier of the grain boundary for the hopping of the charge carriers. Reports are available regarding the B–B interaction predominating over the A–B interaction, which causes the electrical resistance to increase and the dielectric constant to decrease. This depends on the particle size of the synthesized sample.

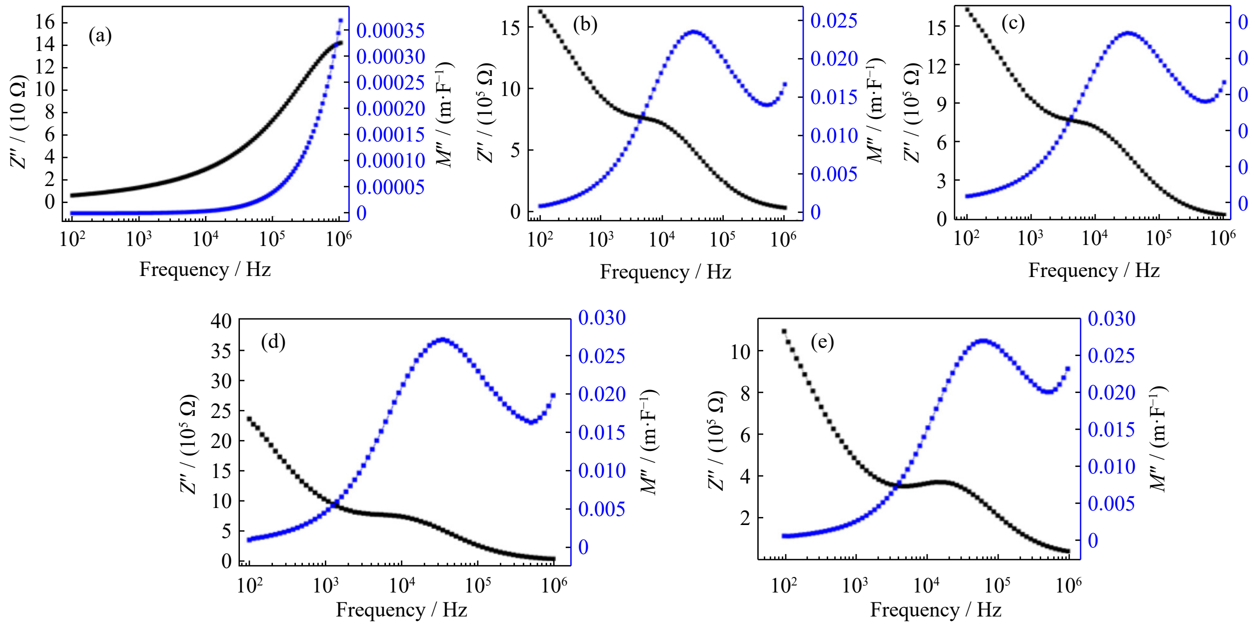

Fig. 12. Combined graph between the imaginary part of the impedance and electric modulus with frequencies of $CoMn_xFe_{(2-x)}O_4$ samples: (a) $x = 0$; (b) $x = 0.05$; (c) $x = 0.10$; (d) $x = 0.15$; (e) $x = 0.20$.

Fig. 13 depicts the Cole–Cole plot of MCFO in the frequency ranging from 100 Hz to 1 MHz with a temperature range of RT to 400°C. This plot was used to analyze the electrical properties of the synthesized material. The semicircular arc in the plot represents either the extrinsic or intrinsic conduction mechanism, wherein the latter is due to grain, while the former is due to the interfacial mechanism. The Cole–Cole diagram illustrates the relationship between real and imaginary impedance. The impedance spectra, along with the contribution of grain, grain boundary, and electrode interface, are observed individually. The plot demonstrates the involvement of grain and grain boundary [41], in which the single semicircle shows the contribution of these properties. Low-frequency semicircles are associated with grain boundary resistance, while high-frequency semicircles are related to grain resistance. When the Mn inclusion increases, the grain boundary resistance increases.

Furthermore, when the temperature increases, the semicircular arcs are comparatively depressed; thus, the intercept of the arc with Z' shifts toward the origin [42]. As previously noted, there are two types of semicircles observed: one is at a low-frequency applied electric field, which indicates the function of grain boundary resistance, and another represents the high-frequency applied electric field area, which indicates the significance of grain resistance.

3.7.3. Electric modulus

Studying the complex electric modulus formula involves analyzing the charge transport mechanism. The relaxation mechanism was used in the present study to investigate the electrical properties of the MCFO series of samples, which

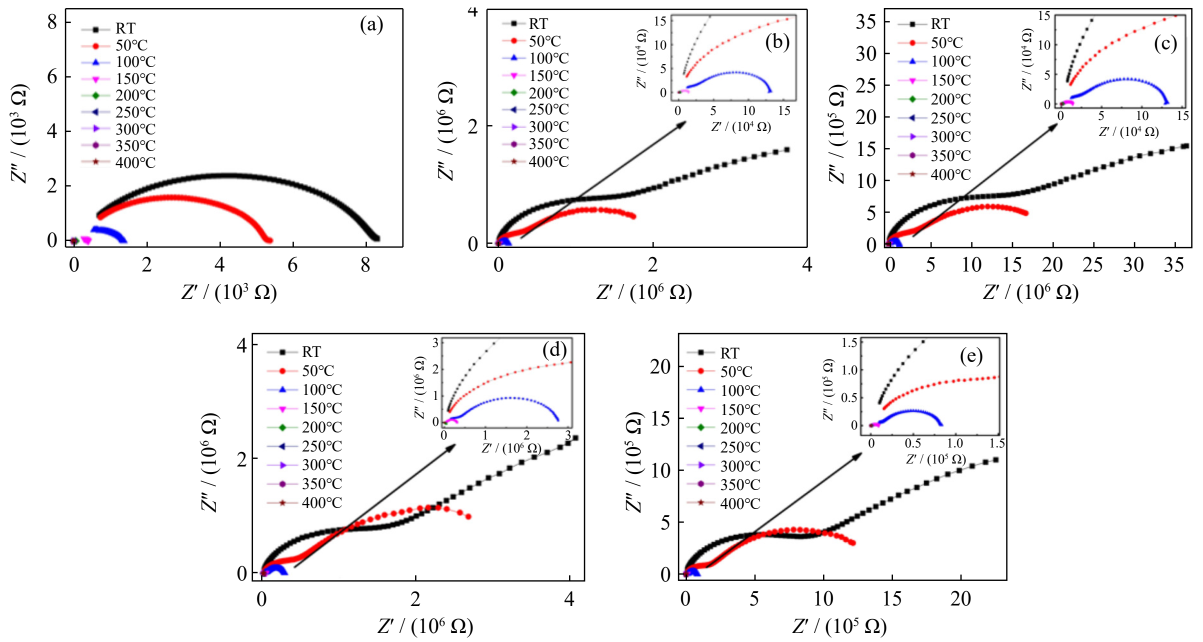

Fig. 13. Nyquist plot of the impedance of $CoMn_xFe_{(2-x)}O_4$ samples at different temperature with x = (a) 0, (b) 0.05, (c) 0.10, (d) 0.15, and (e) 0.20.

we determined from the electric modulus. In general, the complex electric modulus is represented as follows [43]:

$$M = M' + jM'' \tag{9}$$

where M' and M'' represents the real and imaginary part of the electric modulus, respectively.

Fig. 14 presents the real part of the electric modulus (M') at varying frequencies ranging from RT to 400°C. From the figure, we can see that the M' value of all the manganese-doped CFO samples originates from zero for all the temperatures. Thus, we can conclude that the interfacial polarization is suppressed at lower frequency [43]. However, at higher frequencies, the M' value increases and tends to acquire a saturation point. Based on these properties, the synthesized sample exhibits less involvement in the electrode polarization. The graph illustrates that the value of M' approaches zero at the low-frequency region.

Fig. 15 shows the imaginary part of the electric modulus (M'') at different frequencies for a range of temperatures from RT to 400°C. From the modulus, we can obtain information related to the charge transport. Owing to the electrode effect, the M'' value is zero in the lower frequency region. There are peaks observed in the case of MCFO due to the thermal activation of charge carriers, which are shifted to a higher frequency. In the M'' plot, no noticeable peak is observed at high temperatures. The total polarization of the material is associ-

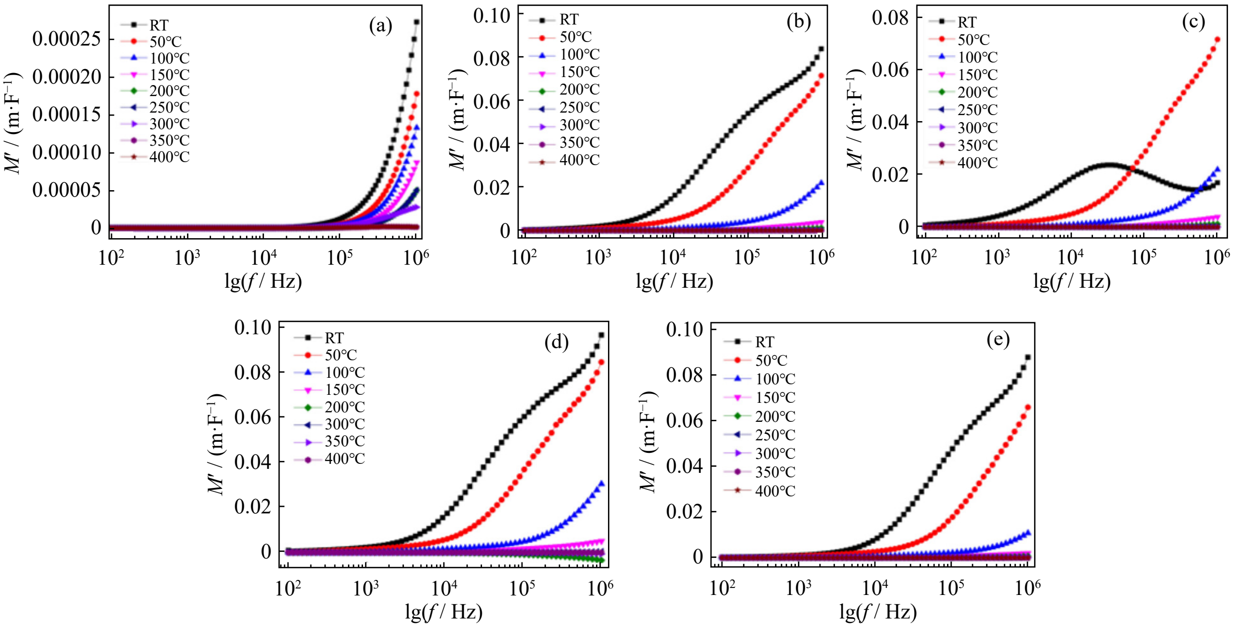

Fig. 14. Variation of the real part of the electric modulus with frequencies at different temperatures of $CoMn_xFe_{(2-x)}O_4$ samples with x = (a) 0, (b) 0.05, (c) 0.10, (d) 0.15, and (e) 0.20.

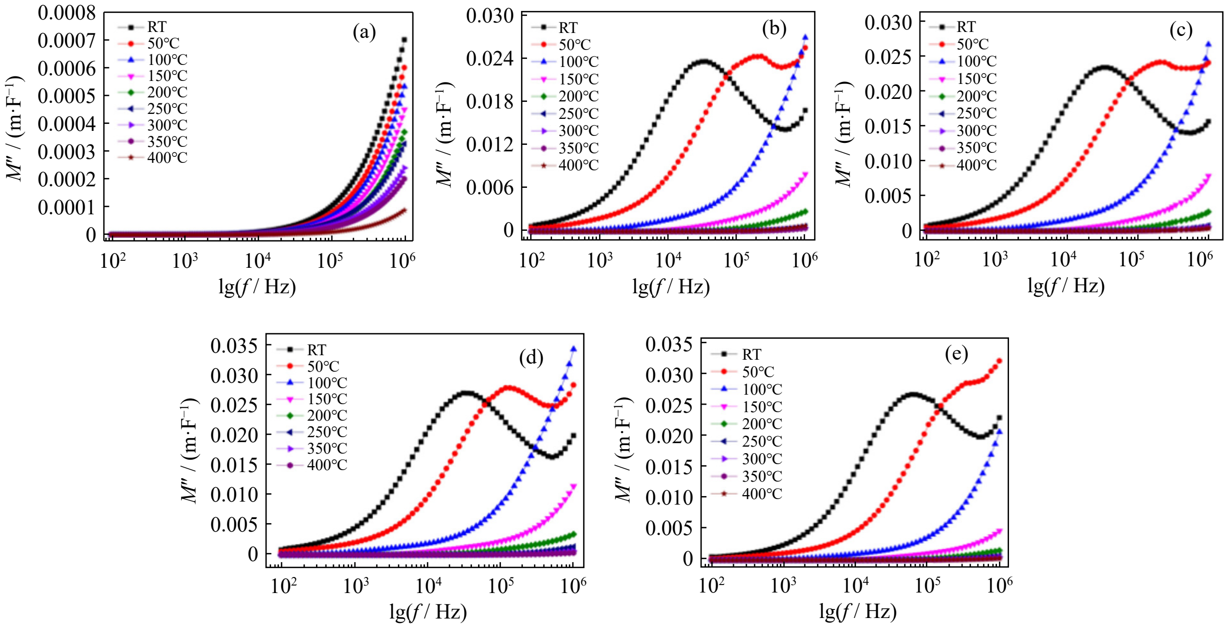

Fig. 15. Variation of the imaginary part of the electric modulus with frequencies at different temperatures of $CoMn_xFe_{(2-x)}O_4$ samples with x = (a) 0, (b) 0.05, (c) 0.10, (d) 0.15, and (e) 0.20.

ated with the charge transport mechanism and the electric relaxation time. Furthermore, the relaxation peaks that appear in the figure represent the long to short-range charge mobility.

3.8. MD property

To analyze the MD effect of the MCFO series sample, the dielectric constant value was measured in both the presence and absence of a magnetic field. The MD property was also investigated in the present study to explore the relationship between dielectric constant and magnetic ordering. Due to the low dielectric and magnetic loss value, moderate saturation magnetization and dielectric constant CFO show sustained MD property. Considering these characteristics, CFO nanoparticles turn out to be effective substrate materials for the development of radar, aerospace telemetry, and telecommunication systems.

Fig. 16 shows the MD% vs. frequency in the range of 100 Hz–1 MHz at the RT, and this characteristic is performed in the 0.1 and 1.3 T magnetic fields. A significant increase in the MD coefficient can be observed in Fig. 16 which is due to the lattice distortion resulting from the lattice strain and magnetostriction effect [44]. The MD% can be calculated as follows:

$$\mathrm{MD\%} = \frac{\varepsilon'(H) - \varepsilon'(0)}{\varepsilon'(0)} \times 100\% \tag{10}$$

where $\varepsilon'(H)$ is dielectric constant in the presence of a magnetic field, and $\varepsilon'(0)$ is dielectric constant without any magnetic field.

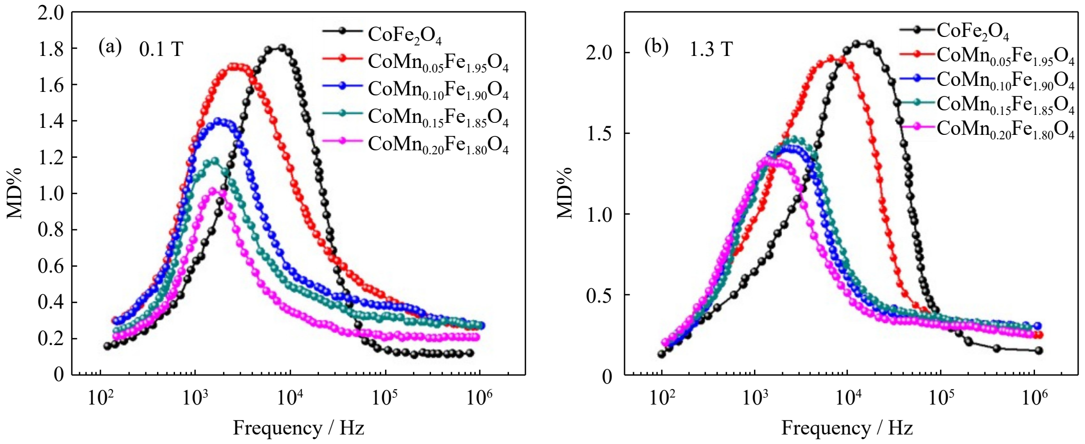

Fig. 16. Variations of the magneto-dielectric coefficients as a function of frequency at RT of $CoMn_xFe_{(2-x)}O_4$ samples at (a) 0.1 and (b) 1.3 T.

When the magnetic field is present, it induces strain in the nanoparticles, which in turn, generates stress and the electric field. In the sample, the MD coupling is positive in nature. Then, as the magnetic field increases, the coupling also increases in number; thus, the MD% at 1.3 T shows a high value compared to that at 0.1 T. When the doping concentration increases, the MD coefficient value decreases. For $CoMn_{0.20}Fe_{1.80}O_4$, the lowest value of MD% has been observed as shown in Table 3.

Table 3. Measured MD% values for $CoMn_xFe_{(2-x)}O_4$ samples

Sample	MD% at 0.1 T	MD% at 1.3 T
$CoFe_2O_4$	1.8	2.0
$CoMn_{0.05}Fe_{1.95}O_4$	1.7	1.9
$CoMn_{0.10}Fe_{1.90}O_4$	1.4	1.4
$CoMn_{0.15}Fe_{1.85}O_4$	1.1	1.4
$CoMn_{0.20}Fe_{1.80}O_4$	1.0	1.3

4. Conclusions

Mn-doped CFO nanoparticles were synthesized vial sol–gel auto-combustion. XRD, FESEM, Raman, and XPS analyses were performed for structural property study. The XRD study confirms the single phase of the synthesized material and that there are no secondary peaks in the spectra. The dielectric constant value is enhanced after the Mn substitution, and minimal loss is observed for $CoMn_{0.20}Fe_{1.80}O_4$, making it suitable for high-frequency storage device applications and transformer cores.

Furthermore, the Cole–Cole plot reveals intrinsic and extrinsic conduction mechanisms in MCFO, with distinct contributions from grain and grain boundary resistances, in which increased Mn inclusion notably raises grain boundary resistance. The absence of M'' values at lower frequencies due to electrode effects and the presence of thermally activated peaks at intermediate frequencies both highlight the temperature-dependent relaxation of charge carriers. The shift of these peaks to higher frequencies with increasing temperature indicates a transition from long- to short-range charge mobility, aligning with the material's polarization behavior and electric relaxation time characteristics.

Additionally, increasing Mn content in CFO raises the residual magnetization (M_r) from 37.77 to 51.89 emu/g while reducing the magnetic moment per unit (Bohr magneton) from $3.07\eta_B$ to $2.80\eta_B$, thus contributing to a decrease in saturation magnetization (M_s) with Mn^{2+} incorporation. The observed increase in the MD coefficient with the applied magnetic field can be attributed to lattice distortion from the strain and magnetostriction effects, with MD% reaching its peak at 1.3 T and diminishing as the doping concentration rises. Meanwhile, under the same condition, $CoMn_{0.20}Fe_{1.80}O_4$ shows the lowest MD%.

Conflict of Interest

The authors declare no conflict of interest.

References

[1] R. Kotnala and J. Shah, Ferrite materials: Nano to spintronics regime, [in] *Handbook of Magnetic Materials*, Vol. 23, 2015, p. 291.

[2] X.Y. Xiang, Z.H. Yang, G. Fang, *et al*., Tailoring tactics for optimizing microwave absorbing behaviors in ferrite materials, *Mater. Today Phys.*, 36(2023), art. No. 101184.

[3] G. Chen, Z.J. Li, L.M. Zhang, *et al*., Mechanisms, design, and fabrication strategies for emerging electromagnetic wave-absorbing materials, *Cell Rep. Phys. Sci.*, 5(2024), No. 7, art. No. 102097.

[4] G.J. Ma, D. Lan, Y. Zhang, *et al*., Microporous cobalt ferrite with bio-carbon loosely decorated to construct multi-functional composite for dye adsorption, anti-bacteria and electromagnetic protection, *Small*, 20(2024), No. 45, art. No. 2404449.

[5] S.J. Salih and W.M. Mahmood, Review on magnetic spinel ferrite (MFe_2O_4) nanoparticles: From synthesis to application, *Heliyon*, 9(2023), No. 6, art. No. e16601.

[6] A.I. Borhan, D. Ghercă, A.R. Iordan, and M.N. Palamaru, Classification and types of ferrites, [in] J.P. Singh, K.H. Chae, R.C. Srivastava, and O.F. Caltun, eds., *Ferrite Nanostructured Magnetic Materials*, Elsevier, Amsterdan, 2023.

[7] N. Adarshgowda, H.S. Bhojya Naik, G. Vishnu, and S. Hareeshanaik, Green synthesized manganese-doped cobalt ferrite photocatalysts for light driven degradation of dye and optoelectronic studies, *Ceram. Int.*, 50(2024), No. 12, p. 22060.

[8] S.J. Zhang, D. Lan, J.J. Zheng, *et al*., Rational construction of heterointerfaces in biomass sugarcane-derived carbon for superior electromagnetic wave absorption, *Int. J. Miner. Metall. Mater.*, 31(2024), No. 12, p. 2749.

[9] X.D. Li, X. Zhu, A.L. Feng, M.M. An, P.T. Liu, and Y.Q. Zu, Electrochemical and surface analysis investigation of corrosion inhibition performance: 6-Thioguanine, benzotriazole, and phosphate salt on simulated patinas of bronze relics, *J. Mater. Res. Technol.*, 29(2024), p. 5667.

[10] B. Dash, K.L. Routray, S. Saha, S. Yoshimura, S. Ratha, and M.K. Rout, Investigation of substitution of nickel cations in cobalt ferrite ($CoFe_2O_4$) nanoparticles and their influence on frequency and temperature dependent dielectric and magnetodielectric properties, *Trans. Electr. Electron. Mater.*, 25(2024), No. 2, p. 232.

[11] K.L. Routray, D. Sanyal, and D. Behera, Dielectric, magnetic, ferroelectric, and Mossbauer properties of bismuth substituted nanosized cobalt ferrites through glycine nitrate synthesis method, *J. Appl. Phys.*, 122(2017), No. 22, art. No. 224104.

[12] M. Satish, H.M. Shashanka, S. Saha, *et al*., Effect of high-anisotropic Co^{2+} substitution for Ni^{2+} on the structural, magnetic, and magnetostrictive properties of $NiFe_2O_4$: Implications for sensor applications, *ACS Appl. Mater. Interfaces*, 15(2023), No. 12, p. 15691.

[13] S. Chakrabarty, A. Dutta, and M. Pal, Effect of Mn and Ni codoping on ion dynamics of nanocrystalline cobalt ferrite: A structure property correlation study, *Electrochim. Acta*, 184(2015), p. 70.

[14] V.P. Thakare, O.S. Game, and S.B. Ogale, Ferromagnetism in metal oxide systems: Interfaces, dopants, and defects, *J. Mater. Chem. C*, 1(2013), No. 8, art. No. 1545.

[15] A.A. Ibiyemi, G.T. Yusuf, O. Akirinola, M. Orojo, B. Osuporu, and J. Lawal, Investigating the magnetic domain structure and photonics characters of singled phased hard ferromagnetic ferrite MFe_3O_4 ($M = Co^{2+}, Zn^{2+}, Cd^{2+}$) compounds, *J. Nig. Soc. Phys. Sci.*, 6(2024), No. 1, art. No. 1909.

[16] R. Jabbar, S.H. Sabeeh, and A.M. Hameed, Structural, dielectric and magnetic properties of Mn^{+2} doped cobalt ferrite nanoparticles, *J. Magn. Magn. Mater.*, 494(2020), art. No. 165726.

[17] M.S. Al Maashani, K.A. Khalaf, A.M. Gismelseed, and I.A. Al-Omari, The structural and magnetic properties of the nano-$CoFe_2O_4$ ferrite prepared by sol–gel auto-combustion technique, *J. Alloy. Compd.*, 817(2020), art. No. 152786.

[18] S. Saha, K.L. Routray, P. Hota, *et al*., Structural, magnetic and

dielectric properties of green synthesized Ag doped $NiFe_2O_4$ spinel ferrite, *J. Mol. Struct.*, 1302(2024), art. No. 137409.

[19] K.L. Routray and S. Saha, Impact of CNTs incorporation on structural, optical and dielectric properties of Ag doped spinel $CoFe_2O_4$ nanohybrid and their photovoltaic possibilities, *J. Inorg. Organomet. Polym. Mater.*, (2024). https://doi.org/10.1007/s10904-024-03137-w

[20] K.L. Routray and S. Saha, Graphene nanoplatelets anchored into Ag doped spinel $CoFe_2O_4$ nanohybrid: Synthesis, structural, electrical, superior dielectric and room temperature induced ferromagnetism performance for high frequency device application, *Diamond Relat. Mater.*, 141(2024), art. No. 110680.

[21] K.L. Routray, S. Saha, and D. Behera, Insight into the anomalous electrical behavior, dielectric and magnetic study of Ag-doped $CoFe_2O_4$ synthesised by okra extract-assisted green synthesis, *J. Electron. Mater.*, 49(2020), No. 12, p. 7244.

[22] S.A. Hassanzadeh-Tabrizi, Precise calculation of crystallite size of nanomaterials: A review, *J. Alloy. Compd.*, 968(2023), art. No. 171914.

[23] X.H. Pang, S.Z. Ji, P. Zhang, *et al.*, Interlayer doping of pseudocapacitive hydrated vanadium oxide via Mn^{2+} for high-performance aqueous zinc-ion battery, *Electrochim. Acta*, 441(2023), art. No. 141810.

[24] I.D. Vlaicu, M. Stefan, C. Radu, D.C. Culita, D. Radu, and D. Ghica, Atomic scale insight into the decomposition of nanocrystalline zinc hydroxynitrate toward ZnO using Mn^{2+} paramagnetic probes, *Front. Chem.*, 11(2023), art. No. 1154219.

[25] P. Kumar, M.C. Mathpal, G.K. Inwati, *et al.*, Study of defect-induced chemical modifications in spinel zinc–ferrites nanostructures by in-depth XPS investigation, *Magnetochemistry*, 9(2023), No. 1, art. No. 20.

[26] S.M. Ansari, D. Phase, Y.D. Kolekar, and C.V. Ramana, Effect of manganese-doping on the chemical and optical properties of cobalt ferrite nanoparticles, *Mater. Sci. Eng. B*, 300(2024), art. No. 117134.

[27] A.L. Kwiatkowski, P.V. Shvets, I.S. Timchenko, *et al.*, Cobalt ferrite nanorods synthesized with a facile “green” method in a magnetic field, *Nanomaterials*, 14(2024), No. 6, art. No. 541.

[28] A. Joshi, R.C. Srivastava, R. Dhyani, and C.S. Joshi, Structural, magnetic, and dielectric properties of yttrium doped cobalt ferrite and their nanocomposites with polythiophene, *J. Magn. Magn. Mater.*, 578(2023), art. No. 170812.

[29] S. Tiwari, G. Lal, H. Bhoi, K. Punia, S. Singh Meena, and S. Kumar, Coexistence of superparamagnetism and superspin glass in non-stoichiometric $Zn_{0.5}Ca_{0.5}Fe_2O_4$ nanoferrite, *J. Magn. Magn. Mater.*, 570(2023), art. No. 170466.

[30] S.O. Aisida, T.C. Chibueze, M.H. Alnasir, *et al.*, Microstructural and magneto-optical properties of $Co_{1-x}Ni_xFe_2O_4$ nanocomposites for hyperthermia applications, *Solid State Sci.*, 136(2023), art. No. 107107.

[31] S.M. Yadav, S. Kumar, M. Kumar, A. Ghosh, and D.S. Saini, High-temperature variable range hopping conduction and dielectric relaxation in $CoFe_2O_4$ ceramic, *Open Ceram.*, 17(2024), art. No. 100517.

[32] X. Fan, T.G. Myers, B.D. Sukra, and G. Gabrielse, Measurement of the electron magnetic moment, *Phys. Rev. Lett.*, 130(2023), No. 7, art. No. 071801.

[33] B. Shi, H.S. Liang, Z.J. Xie, Q. Chang, and H.J. Wu, Dielectric loss enhancement induced by the microstructure of $CoFe_2O_4$ foam to realize broadband electromagnetic wave absorption, *Int. J. Miner. Metall. Mater.*, 30(2023), No. 7, p. 1388.

[34] J.B. Collings, R. Rama-Eiroa, R.M. Otxoa, R.F.L. Evans, and R.W. Chantrell, Generalized form of the magnetic anisotropy field in micromagnetic and atomistic spin models, *Phys. Rev. B*, 107(2023), No. 6, art. No. 064413.

[35] A. Mahmood and A. Maqsood, Temperature and frequency-dependent electrical transport studies of manganese-doped zinc ferrite nanoparticles, *Mater. Sci. Eng. B*, 296(2023), art. No. 116615.

[36] H. Wang and L. Yang, Dielectric constant, dielectric loss, conductivity, capacitance and model analysis of electronic electroactive polymers, *Polym. Test.*, 120(2023), art. No. 107965.

[37] R.J. Sengwa, N. Kumar, and M. Saraswat, Morphological, structural, optical, broadband frequency range dielectric and electrical properties of PVDF/PMMA/$BaTiO_3$ nanocomposites for futuristic microelectronic and optoelectronic technologies, *Mater. Today Commun.*, 35(2023), art. No. 105625.

[38] P.S. Padhi, R.S. Ajimsha, S.K. Rai, *et al.*, Process temperature-dependent interface quality and Maxwell–Wagner interfacial polarization in atomic layer deposited Al_2O_3/TiO_2 nanolaminates for energy storage applications, *Nanoscale*, 15(2023), No. 18, p. 8337.

[39] M. Zulqarnain, S.S. Ali, M.A. Yaqub, *et al.*, Spinel ferrites having conductive grains, resistive interfacial boundaries and relaxation mechanism for possible supercapacitor applications, *Results Phys.*, 61(2024), art. No. 107732.

[40] A. Jain, C. Singh, S.K. Godara, R.B. Jotania, V. Kaur, and A.K. Sood, Investigating grain and grain boundary effects on charge transport and dielectrics in $BaCo_xAl_xFe_{12-2x}O_{19}$ nanoferrites, *Phys. B: Condens. Matter*, 690(2024), art. No. 416211.

[41] F. Eghdami and A. Gholizadeh, A correlation between microstructural and impedance properties of $MnFe_{2-x}Co_xO_4$ nanoparticles, *Phys. B: Condens. Matter*, 650(2023), art. No. 414551.

[42] M.J. Feng, Y. Feng, C.H. Zhang, *et al.*, Enhanced high-temperature energy storage performance of all-organic composite dielectric *via* constructing fiber-reinforced structure, *Energy Environ. Mater.*, 7(2024), No. 2, art. No. e12571.

[43] P. Halder and S. Bhattacharya, Debye to non-Debye type relaxation in MoO_3 doped glassy semiconductors: A portrait on microstructure and electrical transport properties, *Phys. B: Condens. Matter*, 648(2023), art. No. 414374.

[44] L. Zhang, Y.P. Pu, and M. Chen, Complex impedance spectroscopy for capacitive energy-storage ceramics: A review and prospects, *Mater. Today Chem.*, 28(2023), art. No. 101353.